Received October 1, 2020, accepted October 18, 2020, date of publication October 22, 2020, date of current version November 2, 2020.

Digital Object Identifier 10.1109/ACCESS.2020.3033067

Dual-Band Balanced-to-Unbalanced Power Divider With Independent Power Division Ratios

ZIHUI ZHU, ZHONGBAO WANG, (Member, IEEE), JIAN MA, HONGMEI LIU, (Member, IEEE), AND SHAOJUN FANG, (Member, IEEE)

School of Information Science and Technology, Dalian Maritime University, Dalian 116026, China

Corresponding author: Zhongbao Wang (wangzb@dlmu.edu.cn)

This work was supported in part by the National Natural Science Foundation of China under Grant 61871417 and Grant 51809030, in part by the Natural Science Foundation of Liaoning Province under Grant 2019-MS-024 and Grant 2020-MS-127, and in part by the Fundamental Research Funds for the Central Universities under Grant 3132020206 and Grant 3132020207.

ABSTRACT A dual-band balanced to unbalanced power divider with independent power division ratios (PDRs) at two operating frequencies is proposed in this article. The proposed power divider includes a dual-band phase inverter, a grounded resistor, and four transmission-line sections (TLS). By simultaneously changing characteristic impedances and electrical lengths of the four TLS, the independent PDRs are obtained, and the large-signal output port at lower and upper operation bands can be different. Compared to the previous works, it has more flexibility in the power division. Moreover, the closed-form design equations are provided and discussed. To verify the proposed structure, two BTU power dividers operating at 1.0 and 2.0 GHz are designed, fabricated, and measured. The PDRs of the first power divider are −6 and 6 dB for the lower and upper operation bands, respectively. The second power divider has the PDRs of 3 and −6 dB. The measured results are good agreements with the theoretical calculation and electromagnetic simulation.

INDEX TERMS Balanced to unbalanced, dual-band, independent power division ratios, power divider.

I. INTRODUCTION

As a fundamental building block, power dividers have been widely used in microwave applications, such as antenna feeding networks, balanced amplifiers, and mixers. Because of the advantage of high-power applications, Gysel-type power dividers have attracted extensive attention. To meet the requirement for the continuous growth of modern wireless communications, studies on power dividers with various performances have been carried out extensively, including arbitrary power division, bandwidth enhancement, multi-band, and integration with filtering. However, there are challenges from the common-mode noises and radiated electromagnetic (EM) interference for the multifrequency operation modes [1]. Compared to the traditional single-ended components, the balanced ones have the advantages of good common-mode suppression and high immunity to environmental and device electronic noise, such as balanced filter [2]–[4], balanced power divider [5]–[7], and balanced coupler [8]–[10]. Furthermore, the dual-band balanced components can be more adaptable for reducing environmental noises in the multifrequency system.

The associate editor coordinating the review of this manuscript and approving it for publication was Xiu Yin Zhang.

Commonly, multi-port balanced devices add complexity to the overall system, and for a system with both balanced and unbalanced devices, an external balun is required for the connection between conventional power divider and balanced ports, which increases the circuit size. In order to solve this problem, the balanced-to-unbalanced (BTU) power divider is proposed to connect both balanced and unbalanced components [11]. The BTU power divider can divide one pair of differential-mode signals into the isolated single-ended ports with common-mode rejection. In the meantime, unequal power divisions are highly desired [11], especially for feeding networks of antenna arrays and Doherty power amplifiers. By using coupled ring resonators [12], couple lines [13], and π-shaped networks embedded with short-circuited stubs [14], some dual-band BTU equal power dividers are realized. Besides, stepped-impedance transmission lines (TL) are used to realize dual-band BTU unequal power dividers [15]. However, for the existing dual-band BTU power dividers, their power division ratios (PDRs) at the two operating frequencies are always the same, which limits the application for an independent dual-band operation mode.

In this article, a dual-band BTU Gysel-type power divider with independent PDRs at the two operating frequencies is proposed. The proposed power divider includes a dual-band phase inverter, a grounded resistor, and four transmission-line

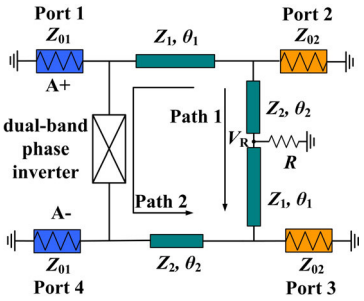

FIGURE 1. The proposed dual-band BTU power divider.

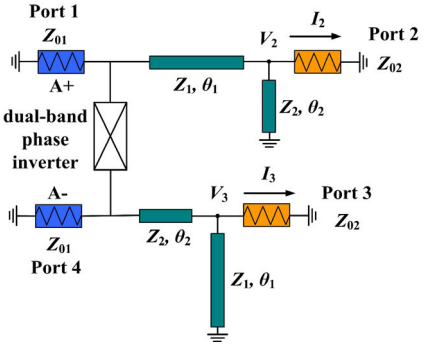

FIGURE 2. Transmission part of the proposed dual-band BTU power divider.

sections (TLS). By simultaneously changing the characteristic impedances and electrical lengths of the TLS, dual-band response with independent PDRs can be achieved. And the closed design formulas are derived. Both the theoretical and experimental results are given and discussed.

II. DESIGN THEORY

The schematic of the proposed dual-band BTU power divider is shown in Figure 1, which consists of a dual-band phase inverter, four TLS (with the characteristic impedance of Z_1 and Z_2), and an isolation resistor R. The isolation resistor is grounded, which makes the created heat sinking of the resistors possible. The balanced input port A comprises of ports 1 and 4 terminated in Z_{01}, and the output ports 2 and 3 are two unbalanced ports terminated in Z_{02}. Frequency ratio n is defined as

$$n = f_2/f_1, \tag{1}$$

where $f_1$and f_2 are the central frequencies of the lower and upper operating bands, respectively. θ_1 and θ_2 are the electrical lengths of the TLS at the central frequency of the lower operating band. Thus, the electrical lengths of the TLS at f_2 can be expressed as $n\theta_1$and $n\theta_2$, respectively.

A. ANALYSIS OF POWER TRANSMISSION FROM INPUT PORT TO OUTPUT PORTS

Due to the fact that when the balanced input port A is excited in differential mode, all the input power is transmitted solely to the terminations at ports 2 and 3 [16], there is no power dissipation in the isolation resistor at the two operating frequencies. The voltage V_R (as shown in Fig. 1) for the resistor R is zero at f_1 and f_2. Fig. 2 gives the simplified power divider.

If the PDR between ports 2 and 3 are k_1^2: 1 at f_1 and k_2^2: 1 at f_2, so it can be obtained that $V_2 = -k_1 V_3$ at f_1 and $V_2 = -k_2 V_3$ at f_2. The voltage relations of the two output branch lines for the differential excitation case (i.e., $V_4 = -V_1$) at f_1 and f_2 can be obtained by using the $ABCD$ matrix.

$$V_1 = V_2 \cos\left(\frac{f}{f_1}\theta_1\right) + V_2 Z_1 \sin\left(\frac{f}{f_1}\theta_1\right) \cot\left(\frac{f}{f_1}\theta_2\right)/Z_2 + \mathrm{j}V_2 Z_1 \sin\left(\frac{f}{f_1}\theta_1\right)/Z_{02}, \tag{2}$$

$$V_4 = -V_1 = V_3 \cos\left(\frac{f}{f_1}\theta_2\right) + V_3 Z_2 \sin\left(\frac{f}{f_1}\theta_2\right) \cot\left(\frac{f}{f_1}\theta_1\right)/Z_1 + \mathrm{j}V_3 Z_2 \sin\left(\frac{f}{f_1}\theta_2\right)/Z_{02}, \tag{3}$$

where $f = f_1$ or f_2. By equating the real and imaginary parts of Equations (2) and (3), respectively, the PDRs at f_1 and f_2 can be derived as

$$k_1 = \frac{Z_2 \sin\theta_2}{Z_1 \sin\theta_1}, \tag{4}$$

$$k_2 = \frac{Z_2 \sin(n\theta_2)}{Z_1 \sin(n\theta_1)}. \tag{5}$$

It can be seen from Equations (4) and (5) that the PDRs of the proposed dual-band BTU power divider are determined by the characteristic impedances and electrical lengths of the TLS.

B. ANALYSIS OF IMPEDANCE MATCHING AND ISOLATION CONDITIONS

To obtain the perfect dual-band impedance matching and isolation conditions, the proposed dual-band BTU power divider between ports 2 and 3 can be separated into two paths, as shown in Fig. 1, and the $ABCD$ matrix of two paths can be obtained as

$$\begin{bmatrix} A & B \\ C & D \end{bmatrix}_{23\_Path1} = \begin{bmatrix} \cos\left(\frac{f}{f_1}\theta_2\right) & \mathrm{j}Z_2 \sin\left(\frac{f}{f_1}\theta_2\right) \\ \mathrm{j}\sin\left(\frac{f}{f_1}\theta_2\right)/Z_2 & \cos\left(\frac{f}{f_1}\theta_2\right) \end{bmatrix} \times \begin{bmatrix} 1 & 0 \\ 1/R & 1 \end{bmatrix} \begin{bmatrix} \cos\left(\frac{f}{f_1}\theta_1\right) & \mathrm{j}Z_1 \sin\left(\frac{f}{f_1}\theta_1\right) \\ \mathrm{j}\sin\left(\frac{f}{f_1}\theta_1\right)/Z_1 & \cos\left(\frac{f}{f_1}\theta_1\right) \end{bmatrix}, \tag{6}$$

$$\begin{bmatrix} A & B \\ C & D \end{bmatrix}_{23\_Path2} = \begin{bmatrix} \cos\left(\frac{f}{f_1}\theta_1\right) & \mathrm{j}Z_1 \sin\left(\frac{f}{f_1}\theta_1\right) \\ \mathrm{j}\sin\left(\frac{f}{f_1}\theta_1\right)/Z_1 & \cos\left(\frac{f}{f_1}\theta_1\right) \end{bmatrix} \times \begin{bmatrix} 1 & 0 \\ 1/Z_{01} & 1 \end{bmatrix} \begin{bmatrix} -1 & 0 \\ 0 & -1 \end{bmatrix} \begin{bmatrix} 1 & 0 \\ 1/Z_{01} & 1 \end{bmatrix} \times \begin{bmatrix} \cos\left(\frac{f}{f_1}\theta_2\right) & \mathrm{j}Z_2 \sin\left(\frac{f}{f_1}\theta_2\right) \\ \mathrm{j}\sin\left(\frac{f}{f_1}\theta_2\right)/Z_2 & \cos\left(\frac{f}{f_1}\theta_2\right) \end{bmatrix} \tag{7}$$

To meet the requirement of perfect isolation ($S_{23} = 0$) and perfect matching at output ports ($S_{22} = 0$ and $S_{33} = 0$) at both central frequencies of the lower and upper operation bands, the following relations need to satisfy [17]

$$B_{23\_Path1} + B_{23\_Path2} = 0, \tag{8}$$

$$Z_{02} = \frac{B_{23\_Path1}}{D_{23\_Path1} - D_{23\_Path2}} = \frac{B_{23\_Path2}}{D_{23\_Path2} - D_{23\_Path1}}. \tag{9}$$

By equating the real and imaginary parts of Equations (8) and (9), the perfect impedance matching and isolation conditions for the proposed power divider can be found as

$$R = Z_{02} = Z_{01}/2, \tag{10}$$

$$\begin{aligned} &2\frac{Z_1}{Z_2}\cos\left(\frac{f}{f_1}\theta_1\right)\cos\left(\frac{f}{f_1}\theta_2\right) \\ &= \frac{Z_1^2}{Z_2^2}\sin\left(\frac{f}{f_1}\theta_1\right)\sin\left(\frac{f}{f_1}\theta_2\right) \\ &\quad + \sin\left(\frac{f}{f_1}\theta_1\right)\sin\left(\frac{f}{f_1}\theta_2\right) - \frac{Z_1^2}{Z_{02}^2}\sin\left(\frac{f}{f_1}\theta_1\right)\sin\left(\frac{f}{f_1}\theta_2\right). \end{aligned} \tag{11}$$

By substituting (4) into (11), the required characteristic impedance Z_1 and Z_2 for perfect impedance matching and isolation at f_1 can be obtained as

$$Z_1 = Z_{02}\sqrt{\frac{\sin^2\theta_2 + k_1^2\sin^2\theta_1 - 2k_1\cos\theta_1\cos\theta_2}{k_1^2\sin^2\theta_1}}, \tag{12}$$

$$Z_2 = Z_{02}\sqrt{\frac{k_1^2\sin^2\theta_1 + \sin^2\theta_2 - 2k_1\cos\theta_1\cos\theta_2}{\sin^2\theta_2}}. \tag{13}$$

Similarly, the required Z_1 and Z_2 for perfect impedance matching and isolation at f_2 are obtained as

$$Z_1 = Z_{02}\sqrt{\frac{\left[\begin{array}{l}\sin^2(n\theta_2) + k_2^2\sin^2(n\theta_1) \\ -2k_2\cos(n\theta_1)\cos(n\theta_2)\end{array}\right]}{k_2^2\sin^2(n\theta_1)}}, \tag{14}$$

$$Z_2 = Z_{02}\sqrt{\frac{\left[\begin{array}{l}k_2^2\sin^2(n\theta_1) + \sin^2(n\theta_2) \\ -2k_2\cos(n\theta_1)\cos(n\theta_2)\end{array}\right]}{\sin^2(n\theta_2)}}. \tag{15}$$

To simultaneously obtain perfect impedance matching and isolation at f_1 and f_2, the required Z_1 in (12) and (14) need to be equal, so Equation (16) is obtained as

$$\frac{\sin^2\theta_2 - 2k_1\cos\theta_1\cos\theta_2}{k_1^2\sin^2\theta_1} = \frac{\sin^2(n\theta_2) - 2k_2\cos(n\theta_1)\cos(n\theta_2)}{k_2^2\sin^2(n\theta_1)} \tag{16}$$

Similarly, Equation (17) is obtained by using (13) and (15).

$$\frac{k_1^2\sin^2\theta_1 - 2k_1\cos\theta_1\cos\theta_2}{\sin^2\theta_2} = \frac{k_2^2\sin^2(n\theta_1) - 2k_2\cos(n\theta_1)\cos(n\theta_2)}{\sin^2(n\theta_2)} \tag{17}$$

There are two unknowns (θ_1 and θ_2) in Equations (16) and (17), their solution can be obtained when frequency ratio n is given.

C. S-PARAMETER ANALYSIS

To derive the standard S-parameter of the proposed power divider, using the topology in Fig. 2 and the *ABCD* matrix can be obtained as

$$\begin{bmatrix} A & B \\ C & D \end{bmatrix}_{14} = \begin{bmatrix} 1 & 0 \\ Y_{L1} & 1 \end{bmatrix}\begin{bmatrix} -1 & 0 \\ 0 & -1 \end{bmatrix}\begin{bmatrix} 1 & 0 \\ Y_{L2} & 1 \end{bmatrix}, \tag{18}$$

with

$$Y_{L1} = \frac{Y_1\left[Y_{02} - \mathrm{j}Y_2\cot\left(\frac{f}{f_1}\theta_2\right) + \mathrm{j}Y_1\tan\left(\frac{f}{f_1}\theta_1\right)\right]}{Y_1 + Y_2\tan\left(\frac{f}{f_1}\theta_1\right)\cot\left(\frac{f}{f_1}\theta_2\right) + \mathrm{j}Y_{02}\tan\left(\frac{f}{f_1}\theta_1\right)}, \tag{19}$$

$$Y_{L2} = \frac{Y_2\left[Y_{02} - \mathrm{j}Y_1\cot\left(\frac{f}{f_1}\theta_1\right) + \mathrm{j}Y_2\tan\left(\frac{f}{f_1}\theta_2\right)\right]}{Y_2 + Y_1\tan\left(\frac{f}{f_1}\theta_2\right)\cot\left(\frac{f}{f_1}\theta_1\right) + \mathrm{j}Y_{02}\tan\left(\frac{f}{f_1}\theta_2\right)}. \tag{20}$$

where $Y_1 = 1/Z_1$ and $Y_{02} = 1/Z_{02}$.

Substituting Equations (10) and (11) into (18), the *ABCD* matrix is simplified as

$$\begin{bmatrix} A & B \\ C & D \end{bmatrix}_{14} = \begin{bmatrix} -1 & 0 \\ -Y_{02} & -1 \end{bmatrix}. \tag{21}$$

Using the conversion of *ABCD* matrix into S-parameters, the S-parameters in terms of ports 1 and 4 are obtained as

$$\begin{bmatrix} S_{11} & S_{14} \\ S_{41} & S_{44} \end{bmatrix} = \begin{bmatrix} -1/2 & -1/2 \\ -1/2 & -1/2 \end{bmatrix}. \tag{22}$$

When either port 1 or 4 is excited, the two divided waves at ports 2 and 3 are 180° out of phase. To realize the PDRs of k_1^2: 1 at f_1 and k_2^2: 1 at f_2, the S_{21} and S_{31} can be obtained with (2) and (3). According to the definition of S-parameters and the use of (4) and (5), the S_{21} and S_{31} are finally simplified as follows,

$$S_{21} = \frac{k_i}{\sqrt{2}\left[k_i(1-\alpha)\cos\left(\frac{f}{f_1}\theta_1\right) + \cos\left(\frac{f}{f_1}\theta_2\right) + k_i\alpha e^{\mathrm{j}\left(\frac{f}{f_1}\theta_2\right)}\right]}, \tag{23}$$

$$S_{31} = \frac{-1}{\sqrt{2}\left[k_i(1-\alpha)\cos\left(\frac{f}{f_1}\theta_1\right) + \cos\left(\frac{f}{f_1}\theta_2\right) + k_i\alpha e^{\mathrm{j}\left(\frac{f}{f_1}\theta_2\right)}\right]}, \tag{24}$$

where

$$\alpha = \sqrt{\frac{\left[\begin{array}{l}\sin^2\left(\frac{f}{f_1}\theta_2\right) + k_i^2\sin^2\left(\frac{f}{f_1}\theta_1\right) \\ -2k_i\cos\left(\frac{f}{f_1}\theta_1\right)\cos\left(\frac{f}{f_1}\theta_2\right)\end{array}\right]}{k_i^2\sin^2\left(\frac{f}{f_1}\theta_1\right)}}, \tag{25}$$

$i = 1$ when $f = f_1$, and $i = 2$ when $f = f_2$.

Considering the perfect isolation between ports 2 and 3 ($S_{ss23} = 0$) and the perfect matching at output ports ($S_{ss22} = 0$ and $S_{ss33} = 0$), the standard scattering matrix S_{std}

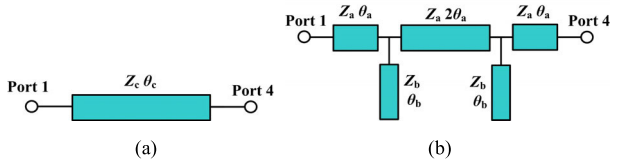

FIGURE 3. (a) Phase inverter (b) Dual-band phase inverter.

is derived as

$$[S_{\text{std}}] = \begin{bmatrix} -1/2 & S_{21} & S_{31} & -1/2 \\ S_{21} & 0 & 0 & -S_{21} \\ S_{31} & 0 & 0 & -S_{31} \\ -1/2 & -S_{21} & -S_{31} & -1/2 \end{bmatrix}. \quad (26)$$

Based on the standard S-parameters (26), the mixed-mode scattering matrix can be obtained as

$$[S_{\text{mm}}] = \begin{bmatrix} S_{\text{ddAA}} & S_{\text{dsA2}} & S_{\text{dsA3}} & S_{\text{dcAA}} \\ S_{\text{sd2A}} & S_{\text{ss22}} & S_{\text{ss23}} & S_{\text{sc2A}} \\ S_{\text{sd3A}} & S_{\text{ss32}} & S_{\text{ss33}} & S_{\text{sc3A}} \\ S_{\text{cdAA}} & S_{\text{csA2}} & S_{\text{csA3}} & S_{\text{ccAA}} \end{bmatrix} = \begin{bmatrix} 0 & \sqrt{2}S_{21} & \sqrt{2}S_{31} & 0 \\ \sqrt{2}S_{21} & 0 & 0 & 0 \\ \sqrt{2}S_{31} & 0 & 0 & 0 \\ 0 & 0 & 0 & -1 \end{bmatrix}, \quad (27)$$

where S_{sd} denotes differential-mode to single-ended transmission coefficients. S_{sc} denotes common-mode to single-ended suppression coefficients. S_{dd}, S_{cc}, and S_{cd} denote differential return loss (DRL), common-mode reflection, and differential-mode to common-mode conversion coefficient, respectively. S_{ss} means single-ended S-parameter.

D. DUAL-BAND PHASE INVERTER

The phase inverter and its dual-band equivalent structure are given in Fig. 3. The transforming relationship between two circuits can be derived [18],

$$\theta_{\text{a}} = \frac{\pi}{1+n} \quad (28)$$

$$\theta_{\text{b}} = \frac{2\pi}{1+n} \quad (29)$$

$$Z_{\text{a}} = \frac{Z_{\text{c}}}{\tan\theta_{\text{a}}} \quad (30)$$

$$Z_{\text{b}} = \frac{Z_{\text{a}}\sin\theta_{\text{a}}\cos\theta_{\text{a}}\tan\theta_{\text{b}}}{\cos^2\theta_{\text{a}} - \sin^2\theta_{\text{a}}} \quad (31)$$

where θ_{a} and θ_{b} are the electrical lengths at f_1.

Fig. 4 gives the effects of the phase inverter characteristic impedance Z_{c} on the mixed S-parameter. It can be seen from Fig. 4 that the bandwidth of $|S_{\text{sd2A}}|$ and $|S_{\text{ddAA}}|$ will be improved when Z_{c} is increased. However, a larger Z_{c} leads to a narrower bandwidth of $|S_{\text{ccAA}}|$ and $|S_{\text{sc2A}}|$. Moreover, the characteristic impendences calculated with (30) and (31) need to be realizable. Therefore, Z_{c} is finally chosen as 60 Ω.

E. PARAMETERS ANALYSIS

Based on the previous theoretical analysis, the design parameters of the proposed power divider can be calculated with the given PDRs and frequency ratio n by using Equations (10), and (14)–(17). Fig. 5 shows the calculated electrical lengths and characteristic impedances for specific PDRs. Limited by the realizable characteristic impedance range of 20-120 Ω for microstrip lines, the frequency ratio for the proposed circuit can be selected from 1.4 to 2.8 with the largest PDR of 6 dB.

Three sets of design parameters are calculated with the frequency ratio $n = 2$. In the first case for the PDRs of −6 and 6 dB, Z_1, Z_2, θ_1, and θ_2 are calculated as 81.99 Ω, 55.6 Ω, 80.08°, and 46.7°. In the second case for the PDRs of 3 dB

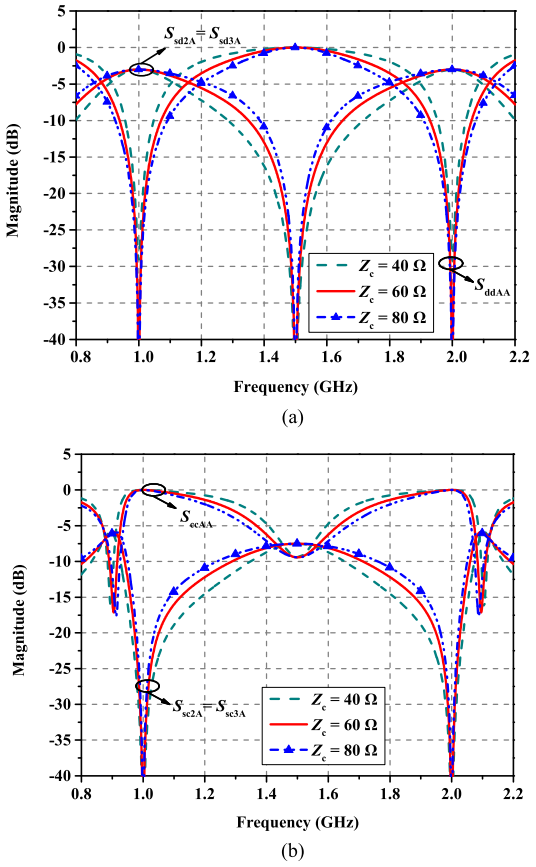

FIGURE 4. Effect of Z_{c} on (a) $|S_{\text{ddAA}}|$, $|S_{\text{sd2A}}|$ and $|S_{\text{sd3A}}|$ (b) $|S_{\text{ccAA}}|$ and $|S_{\text{sc2A}}|$.

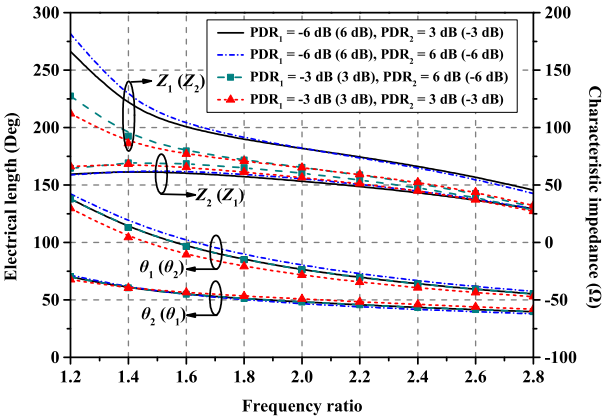

FIGURE 5. The electrical length and the characteristic impedance versus the frequency ratio.

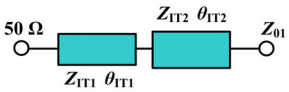

FIGURE 6. Two-section impedance transformer.

and −6 dB, Z_1, Z_2, θ_1, and θ_2 are calculated as 60.21 Ω, 65.26 Ω, 48.21°, and 76.33°. For the case of 6 and −3 dB, Z_1, Z_2, θ_1, and θ_2 are calculated as 53.44 Ω, 81.84 Ω, 48.21°, and 76.33°. In the three cases, the other parameters are all set as $Z_{02} = Z_1 = R = 50\ \Omega$, $Z_{01} = 2Z_{02} = 100\ \Omega$. $\theta_a = 60°\theta_b = 120°$, $Z_a = 34\ \Omega$ and $Z_b = 51\ \Omega$.

A two-section impedance transformer given in Fig. 6 is applied for matching Z_{01} to the standard 50-Ω port, characteristic impedance values and electrical lengths are given as [19]

$$\theta_{IT1} = \theta_{IT2} = \frac{\pi}{1+n} \tag{32}$$

$$Z_{IT1} = \sqrt{\frac{Z_{02}(Z_{01}-Z_{02})}{2\tan^2\theta_{IT1}} + \sqrt{\left[\frac{Z_{02}(Z_{01}-Z_{02})}{2\tan^2\theta_{IT1}}\right]^2 + Z_{02}^3 Z_{01}}} \tag{33}$$

$$Z_{IT2} = Z_{02}Z_{01}/Z_{IT1} \tag{34}$$

where θ_{IT1} and θ_{IT2} are electrical lengths at f_1. For the frequency ratio $n = 2$, the values are given as $\theta_{IT1} = \theta_{IT2} = 60°$, $Z_{IT1} = 63.06\ \Omega$, and $Z_{IT2} = 79.29\ \Omega$.

The mixed scattering parameters for the three cases are given in Figs. 7-9. The $|S_{sd2A}|$ in Fig. 7(a) at the operating frequencies of 1.0 and 2.0 GHz are −6.97 and −0.99 dB, the $|S_{sd3A}|$ are −0.97 and −6.97 dB, leading to the PDRs at the two operating frequencies of −6 and 6 dB, respectively.

The $|S_{sd2A}|$ in Fig. 8(a) at the two operating frequencies are −0.97 and −4.77 dB, the $|S_{sd3A}|$ are −6.98 and −1.76 dB, leading to the PDRs at the two operating frequencies of 6 and −3 dB, respectively.

The $|S_{sd2A}|$ in Fig. 9(a) at the two operating frequencies are −1.76 and −6.98 dB, the $|S_{sd3A}|$ are −4.76 and −0.97 dB, leading to the PDRs of 3 and −6 dB, respectively. Figs. 7-9 show that independent PDRs at the two operating frequencies are obtained.

When the port *A* is excited in the common mode, $|S_{ccAA}|$ at the operating frequencies of 1.0 and 2.0 GHz are always 0 dB, and the transmission parameters of $|S_{cc2A}|$ and $|S_{cc3A}|$ are all less than −60 dB, implying that no common-mode power transfers from the port *A* to ports 2 and 3, as shown in Figs. 7-9. For the three cases, the phase differences between S_{sd3A} and S_{sd2A} at the two operating frequencies of 1.0 and 2.0 GHz are 180°. The dual-band out-of-phase characteristics at two unbalanced output ports are obtained. Figs. 7-9 also show that perfect impedance matching ($S_{ddAA} = 0$, $S_{ss22} = 0$, and $S_{ss33} = 0$) and isolation ($S_{ss23} = 0$) at both operating frequencies are simultaneously obtained for various PDRs, which verifies the previous theoretical analysis.

Based on the foregoing analysis studies, the following procedures shown in Figure 10 are suggested to design the proposed dual-band BTU power divider.

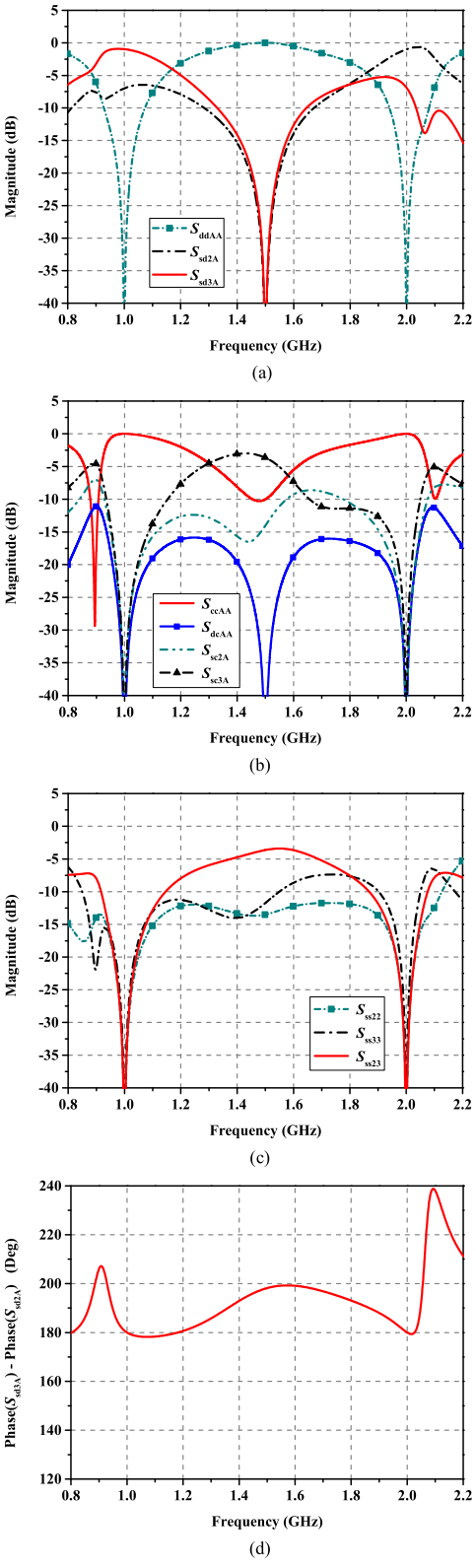

FIGURE 7. Performances of the proposed BTU power divider with PDR1 = −6 dB, PDR2 = 6 dB. (a) $|S_{sd2A}|$, $|S_{sd3A}|$ and $|S_{ddAA}|$. (b) $|S_{ccAA}|$, $|S_{sc2A}|$, $|S_{sc3A}|$ and $|S_{dcAA}|$. (c) Output ports isolation and return loss. (d) Unwrapped phase difference between the output ports.

1) Determine the frequency ratio n and the desired PDRs at f_1 and f_2 referring to Figure 5.

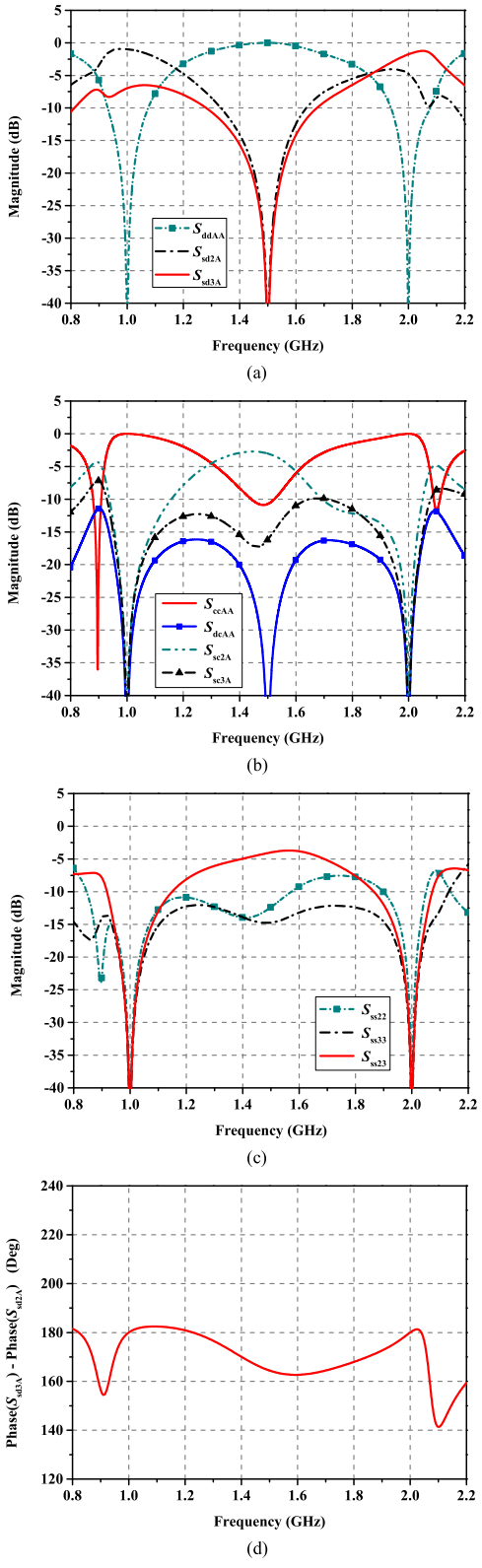

FIGURE 8. Performances of the proposed BTU power divider with PDR1 = 6 dB, PDR2 = −3 dB. (a) $|S_{sd2A}|$, $|S_{sd3A}|$ and $|S_{ddAA}|$. (b) $|S_{ccAA}|$, $|S_{sc2A}|$, $|S_{sc3A}|$ and $|S_{dcAA}|$. (c) Output ports isolation and return loss. (d) Unwrapped phase difference between the output ports.

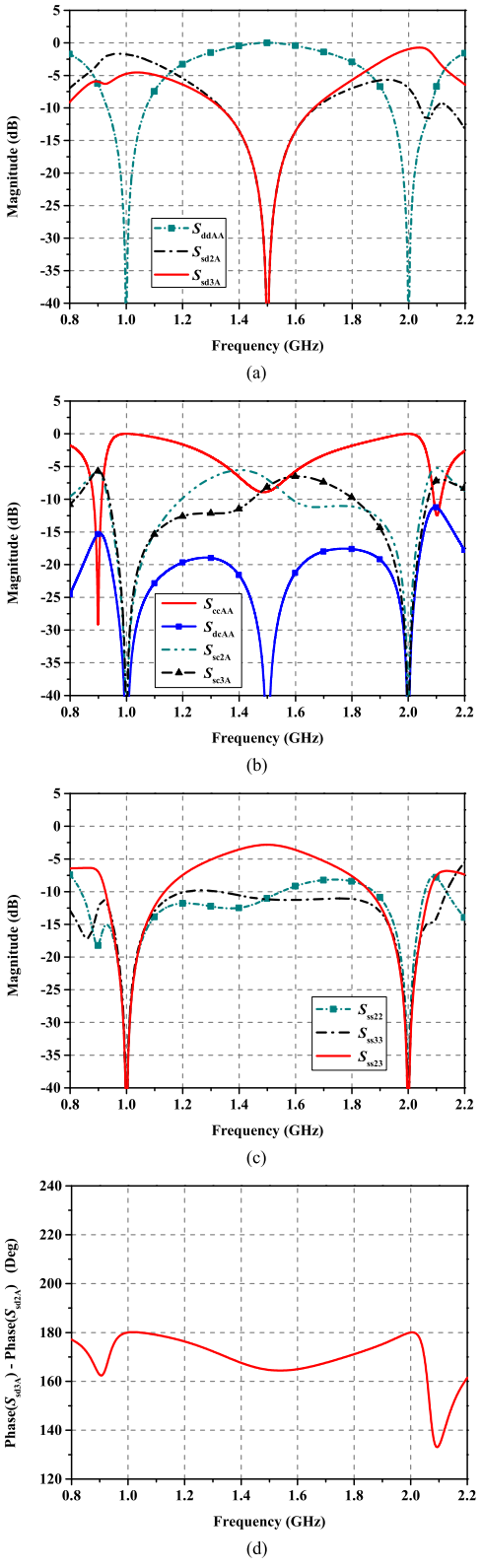

FIGURE 9. Performances of the proposed BTU power divider with PDR1 = 3 dB, PDR2 = −6 dB. (a) $|S_{sd2A}|$, $|S_{sd3A}|$ and $|S_{ddAA}|$. (b) $|S_{ccAA}|$, $|S_{sc2A}|$, $|S_{sc3A}|$ and $|S_{dcAA}|$. (c) Output ports isolation and return loss. (d) Unwrapped phase difference between the output ports.

2) Calculate the electrical lengths θ_1 and θ_2 using (16) and (17).

3) Calculate the characteristic impedances Z_1 and Z_2 using (12) and (13).

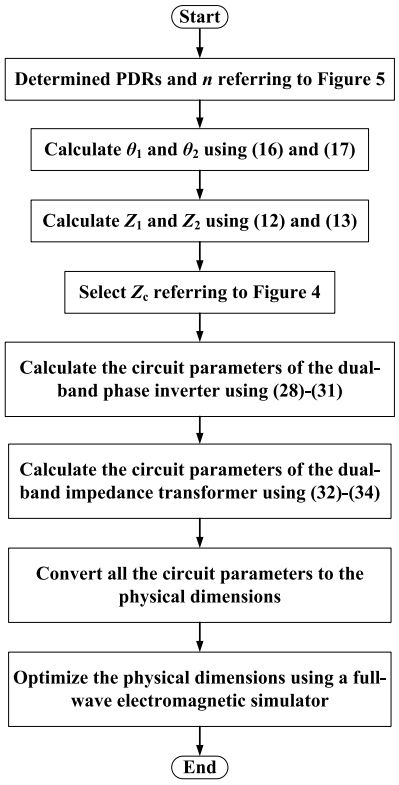

FIGURE 10. The flowchart of the procedures to design the proposed dual-band BTU power divider.

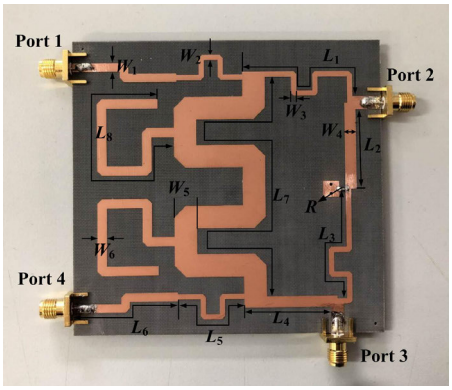

FIGURE 11. Photograph of Design 1.

TABLE 1. Dimensions of Design 1 (unit: mm; refer to Fig. 11).

W_1	W_2	W_3	W_4	W_5	W_6	L_1
2.69	1.27	3.04	2.65	7.1	2.98	46.22
L_2	L_3	L_3	L_5	L_6	L_7	L_8
25.95	39.73	27.95	29	33.3	126.4	70

4) Select the characteristic impedance Z_c referring to Figure 4.

5) Calculate the circuit parameters of the dual-band phase inverter using (28)-(31)

6) Calculate the circuit parameters of the dual-band impedance transformer using (32)-(34).

7) Convert all the circuit parameters to the physical dimensions using the TL synthesis tool ADS Linecalc.

8) Optimize the physical dimensions using a full-wave electromagnetic simulator ANSYS HFSS.

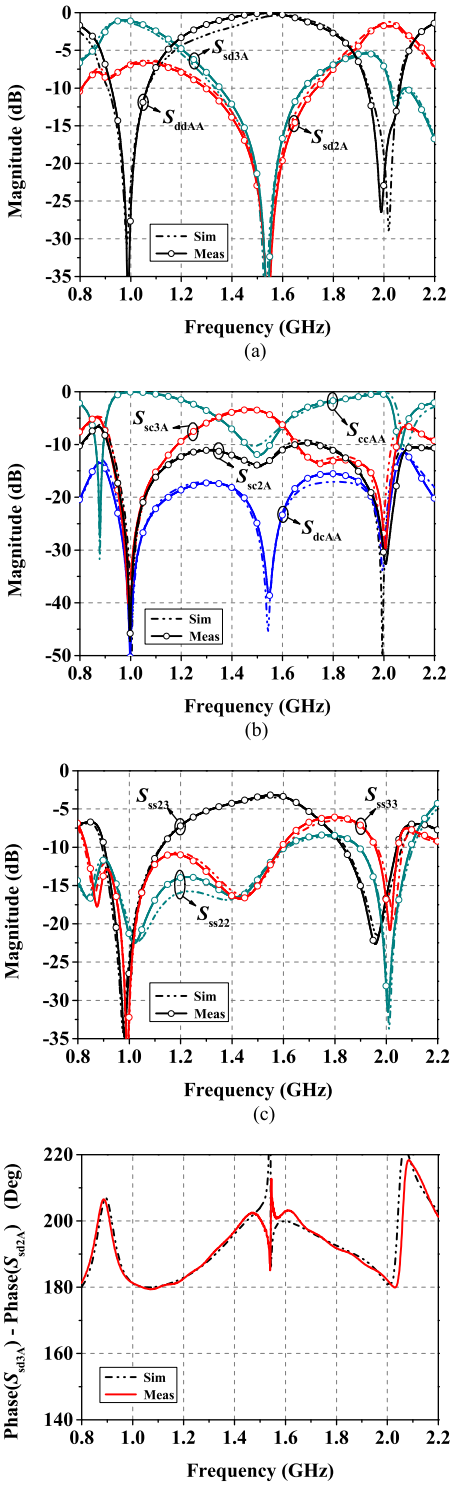

FIGURE 12. Performances of Design 1 (a) $|S_{sd}|$ and $|S_{ddAA}|$ (b) $|S_{sc}|$, $|S_{ccAA}|$ and $|S_{dcAA}|$ (c) Output ports isolation and return loss (d) Unwrapped phase difference between output ports.

III. CIRCUIT LAYOUT AND IMPLEMENTATION

For experimental demonstration, the proposed theory and predicted performance are verified by a microstrip dual-band BTU power divider with the PDRs of −6 and 6 dB (Design 1), and a power divider with the PDRs of 3 and −6 dB (Design 2). Both power dividers are designed with the operating fre-

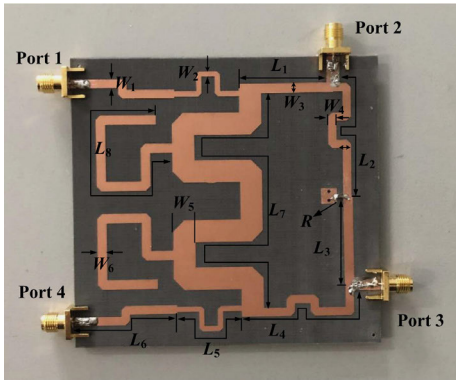

FIGURE 13. Photograph of Design 2.

quencies of $f_1 = 1.0$ GHz and $f_2 = 2.0$ GHz, which are implemented on PTFE/woven-glass substrate with a relative permittivity of 2.65 and thickness of 1.5 mm.

A. DESIGN 1

Based on the design procedures in Figure 10, the main circuit parameters for the PDRs of −6 and 6 dB are calculated as $\theta_1 = 80.08°$, $\theta_2 = 46.7°$, $Z_1 = 81.99\ \Omega$, $Z_2 = 55.6\ \Omega$, $\theta_a = 60°$, $\theta_b = 120°$, $Z_a = 34\ \Omega$, $Z_b = 51\ \Omega$, $\theta_{IT1} = \theta_{IT2} = 60°$, $Z_{IT1} = 63.06\ \Omega$, $Z_{IT2} = 79.29\ \Omega$ and $R = 50\ \Omega$. The photograph of the fabricated circuit for Design 1 is given in Fig. 11. The final dimensions of the circuit are given in Table 1. The overall size is 0.48 $\lambda_g \times 0.45\ \lambda_g$, where λ_g is the guide wavelength of 50-Ω TLs at the first operating frequency. The simulated and measured performances of the proposed dual-band BTU power divider (Design 1) are shown in Figure 12.

The measured $|S_{sd2A}|$ at f_1 and $f_2$are −6.91 and −1.73 dB, respectively, and $|S_{sd3A}|$ are −1.33 and −6.99 dB as shown in Fig. 12(a). The measured DRL at f_1 is 23.0 dB, and the −10-dB fractional bandwidth (FBW) is about 16.0% from 0.909 to 1.067 GHz, while the measured DRL at f_2 is 19.0 dB with the DRL less than −10 dB from 1.941 to 2.058 GHz (5.9%). Besides, the common-mode suppression (CMS) of output ports 2 and 3 are given as $|S_{sc2A}|$ and $|S_{sc3A}|$ in Fig. 12(b), and the measured $|S_{sc2A}|$ and $|S_{sc3A}|$ are −35.6 and −44.1 dB at f_1, −27.5 and −30.8 dB at f_2, respectively. At the lower band, the CMS has a −10-dB bandwidth from 0.914 to 1.190 GHz, with $|S_{ccAA}|$ greater than −3.95 dB, while the CMS at the upper band has a −10-dB bandwidth from 1.732 to 2.080 GHz, in which $|S_{ccAA}|$ is greater than −2.87 dB.

The $|S_{ss22}|$ and $|S_{ss33}|$ in Fig. 12(c) shows that the output ports 2 and 3 have a wide 10-dB impedance matching bandwidth at the lower frequency band. The measured isolation ($|S_{ss23}|$) greater than 10 dB is from 0.894 to 1.123 GHz (22.7%) with the value of 24.4 dB at f_1, and 1.841 to 2.065 GHz (11.5%) with the value of 17.6 dB at f_2, respectively. Because the difference between theoretical resistance and chip resistor value, and the stronger parasitic effect around the resistor at the upper band, the isolation at the upper band is smaller than that at the lower band. Furthermore, the measured phase differences between output ports 2 and 3 are 181.2° at f_1 and 182.1° at f_2, as shown in Fig. 12(d).

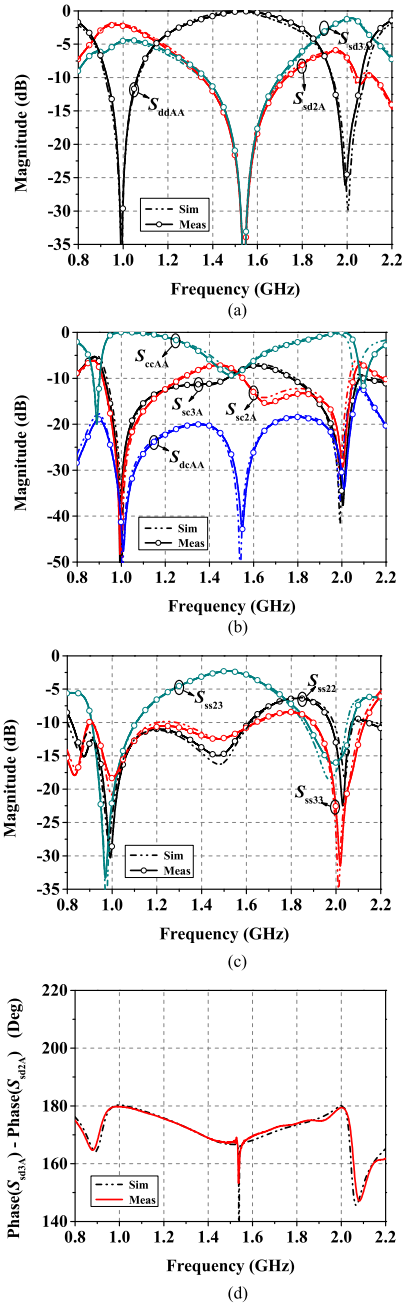

FIGURE 14. Performances of Design 2 (a) $|S_{sd}|$ and $|S_{ddAA}|$ (b) $|S_{sc}|$, $|S_{ccAA}|$ and $|S_{dcAA}|$ (c) Output ports isolation and return loss (d) Unwrapped phase difference between output ports.

TABLE 2. Dimensions of Design 2 (unit: mm; refer to Fig. 13).

W_1	W_2	W_3	W_4	W_5	W_6	L_1
2.69	1.27	3.04	2.65	7.1	2.98	27.95
L_2	L_3	L_3	L_5	L_6	L_7	L_8
40.75	28	44.5	29	33.3	126.4	70

B. DESIGN 2

In Design 2 for the PDRs of 3 and −6 dB, most of the circuit element values are the same as Design 1, except for the values of the TLS characteristic impedances and electrical lengths.

TABLE 3. Performance comparisons.

Ref.	f_1 & f_2 (GHz)	PDR (dB)	FBW (%)	DRL (dB) @f_1&f_2	CMS (dB) @f_1&f_2	Isolation (dB)@ f_1 & f_2	Size ($\lambda_g \times \lambda_g$)
[11]	2.0	3	~43	~25	>20	~18	0.73×0.45
[12]	2.82 & 3.22	0 & 0	7.9 & 6.9	20 & 27	>15 & >15	19 & 18	~0.78×0.49
[13]	0.9 & 1.8	0 & 0	11.9 & 5.9	24 & 25	22 & 17	28 & 22.5	~0.69×0.57
[14]	1.0 & 2.2	0 & 0	30 & 13.6	22 & 28	15.3 &14.7	35 & 37	0.41×0.34
[15]	1.0 & 6.4	0 & 0	53 & 7.3	27 & 28	38.3 & 28.2	22 & 14	0.75×0.51
Design 1	**1.0 & 2.0**	**-6 & 6**	**16.0 & 5.9**	**23.0 & 19.0**	**35.6 & 27.5**	**24.4 & 17.6**	**0.48×0.45**
Design 2	**1.0 & 2.0**	**3 & -6**	**15.1 & 6.5**	**27.1 & 24.1**	**36.3 & 28.4**	**21.9 & 16.3**	**0.48×0.45**

PDR: Power division ratio. FBW: Fractional bandwidth. DRL: Differential return loss. CMS: Common mode suppression.

The electrical lengths and characteristic impedances of the four TLS are calculated as $\theta_1 = 48.21°$, $\theta_2 = 76.33°$, $Z_1 = 60.21\ \Omega$, and $Z_2 = 65.26\ \Omega$. The photograph of the fabricated circuit for Design 2 is given in Figure 13. The final dimensions of the circuit are given in Table 2. The overall size is 0.48 $\lambda_g \times 0.45\ \lambda_g$.

The measured $|S_{sd2A}|$ at f_1 and $f_2$are -2.23 and -7.06 dB, respectively, and $|S_{sd3A}|$ are -4.65 and -1.55 dB as shown in Fig. 14(a). The measured DRL at f_1 is 27.1 dB, and the -10-dB FBW is about 15.1% from 0.919 to 1.069 GHz, while the measured DRL at f_2 is 24.1 dB with the DRL less than -10 dB from 1.932 to 2.062 GHz (6.5%). The measured $|S_{sc2A}|$ and $|S_{sc3A}|$ are -36.3 and -38.8 dB at f_1, -35.2 and -28.4 dB at f_2, respectively, as shown in Fig. 14(b). Moreover, the CMS at the lower band has the -10-dB bandwidth ranging from 0.916 to 1.27 GHz with $|S_{ccAA}|$ greater than -4.52 dB. At the upper band, the -10-dB bandwidth of CMS is obtained from 1.770 to 2.098 GHz, in which $|S_{ccAA}|$ is greater than -4.3 dB.

It is seen from Fig. 14(c) that the measured isolation ($|S_{ss23}|$) at f_1 and f_2 are 21.9 and 16.3 dB, respectively. The measured isolation is greater than 10 dB from 0.909 to 1.108 GHz (19.7%) and 1.867 to 2.074 GHz (10.5%). Furthermore, the measured phase differences between output ports 2 and 3 at f_1 and f_2 are 179.7° and 180.1°, respectively, as shown in Fig. 14(d).

The comparison of the proposed dual-band BTU power divider with previous works is summarized in Table 3. Compared with [11]–[15], the proposed dual-band BTU power divider has more flexibility of the power division, such as arbitrary PDRs, the lower and upper band with different large signal output ports. The size of the proposed BTU power divider is less than that of [11]–[13], and [15]. Furthermore, good CMS and large DRL are also obtained for various PDRs.

IV. CONCLUSION

In this article, a dual-band BTU power divider with independent PDRs has been presented. The large signal output port at lower and upper operation bands can be different. And the proposed dual-band BTU power divider can be easily synthesized with the prescribed arbitrary PDRs. In addition, the proposed dual-band BTU power divider is a Gysel-type power divider, which is also suitable for high power applications.

REFERENCES

[1] H. Zhang, L. Yang, S. Wang, and J. Puukko, "Common-mode EMI noise modeling and reduction with balance technique for three-level neutral point clamped topology," *IEEE Trans. Ind. Electron.*, vol. 64, no. 9, pp. 7563–7573, Sep. 2017.

[2] Y. Wu, Z. Zhuang, M. Kong, L. Jiao, Y. Liu, and A. A. Kishk, "Wideband filtering unbalanced-to-balanced independent impedance-transforming power divider with arbitrary power ratio," *IEEE Trans. Microw. Theory Techn.*, vol. 66, no. 10, pp. 4482–4496, Oct. 2018.

[3] W. Zhang, Y. Wu, Y. Liu, C. Yu, A. Hasan, and F. M. Ghannouchi, "Planar wideband differential-mode bandpass filter with common-mode noise absorption," *IEEE Microw. Wireless Compon. Lett.*, vol. 27, no. 5, pp. 458–460, May 2017.

[4] W. Feng, X. Ma, W. Che, and Y. Wu, "Narrow-band balanced filtering network using coupled lines loaded with stubs," *Electron. Lett.*, vol. 54, no. 6, pp. 366–367, 2018.

[5] X. Gao, W. Feng, and W. Che, "High-selectivity wideband balanced filters using coupled lines with open/shorted stubs," *IEEE Microw. Wireless Compon. Lett.*, vol. 27, no. 3, pp. 260–262, Mar. 2017.

[6] B. Xia, L.-S. Wu, and J. Mao, "A new balanced-to-balanced power divider/combiner," *IEEE Trans. Microw. Theory Techn.*, vol. 60, no. 9, pp. 2791–2798, Sep. 2012.

[7] B. Xia, L.-S. Wu, S.-W. Ren, and J.-F. Mao, "A balanced-to-balanced power divider with arbitrary power division," *IEEE Trans. Microw. Theory Techn.*, vol. 61, no. 8, pp. 2831–2840, Aug. 2013.

[8] M. Li, Y. Wu, L. Jiao, L. Ma, W. Wang, and Y. Liu, "A planar balanced-to-balanced power divider with wideband filtering responses and common-mode suppressions," *IEEE Access*, vol. 6, pp. 42057–42065, 2018.

[9] L. Jiao, Y. Wu, W. Zhang, M. Li, Y. Liu, Q. Xue, and Z. Ghassemlooy, "Design methodology for six-port equal/unequal quadrature and rat-race couplers with balanced and unbalanced ports terminated by arbitrary resistances," *IEEE Trans. Microw. Theory Techn.*, vol. 66, no. 3, pp. 1249–1262, Mar. 2018.

[10] L. Li, J.-F. Mao, and L.-S. Wu, "A single-ended-to-balanced impedance-transforming branch-line coupler with arbitrary power division ratio," *IEEE Trans. Microw. Theory Techn.*, vol. 67, no. 3, pp. 949–956, Mar. 2019.

[11] A. N. Yadav and R. Bhattacharjee, "Balanced to unbalanced power divider with arbitrary power ratio," *IEEE Microw. Wireless Compon. Lett.*, vol. 26, no. 11, pp. 885–887, Nov. 2016.

[12] W. Feng, M. Hong, and W. Che, "Dual-band balanced-to-unbalanced filtering power divider by coupled ring resonators," *Electron. Lett.*, vol. 52, no. 22, pp. 1862–1864, Oct. 2016.

[13] W. Zhang, Y. Wu, C. Yu, S. Li, W. Wang, M. Su, and Y. Liu, "Dual-band balanced-to-unbalanced power divider with inherent impedance transformation," *Electromagnetics*, vol. 37, no. 2, pp. 127–137, Feb. 2017.

[14] Z. Zhuang, Y. Wu, and Y. Liu, "Dual-band filtering out-of-phase balanced-to-single-ended power divider with enhanced bandwidth," *AEU-Int. J. Electron. Commun.*, vol. 82, pp. 341–345, Dec. 2017.

[15] Z. Zhuang, Y. Wu, M. Kong, W. Wang, and Y. Liu, "Dual-band filtering balanced-to-unbalanced impedance-transforming power divider with high frequency ratio and arbitrary power division," *IEEE Access*, vol. 6, pp. 12710–12717, 2018.
[16] F. Lin, Q.-X. Chu, Z. Gong, and Z. Lin, "Compact broadband gysel power divider with arbitrary power-dividing ratio using microstrip/slotline phase inverter," *IEEE Trans. Microw. Theory Techn.*, vol. 60, no. 5, pp. 1226–1234, May 2012.
[17] Y. Wu, Y. Liu, and S. Li, "A modified gysel power divider of arbitrary power ratio and real terminated impedances," *IEEE Microw. Wireless Compon. Lett.*, vol. 21, no. 11, pp. 601–603, Nov. 2011.
[18] B. Xia and J.-F. Mao, "A new dual band balanced-to-balanced power divider," *Prog. Electromagn. Res. C*, vol. 37, pp. 53–66, Jan. 2013.
[19] C. Monzon, "A small dual-frequency transformer in two sections," *IEEE Trans. Microw. Theory Techn.*, vol. 51, no. 4, pp. 1157–1161, Apr. 2003.

ZIHUI ZHU received the B.Eng. degree in electronic information science and technology from Dalian Maritime University (DMU), Liaoning, China, in 2016, where he is currently pursuing the Ph.D. degree in information and communication engineering. His current research interests include power divider and balanced components.

ZHONGBAO WANG (Member, IEEE) received the Ph.D. degree in communication and information systems from Dalian Maritime University (DMU), China, in 2012. He is currently an Associate Professor with the School of Information Science and Technology, DMU. From 2014 to 2018, he was a Postdoctoral Fellow with the Beijing University of Posts and Telecommunications, China. From 2019 to 2020, he was a Visiting Scholar with the Department of Electrical and Computer Engineering, National University of Singapore, Singapore. His current research interests include passive RF components, patch antennas, and microwave technology using artificial intelligence. He has authored or coauthored two books and over 80 articles in journals and conferences. He is currently serving as a Technical Reviewer for the IEEE TRANSACTIONS ON MICROWAVE THEORY AND TECHNIQUES, the IEEE TRANSACTIONS ON CIRCUITS AND SYSTEMS, the IEEE TRANSACTIONS ON INDUSTRIAL ELECTRONICS, the IEEE MICROWAVE AND WIRELESS COMPONENTS LETTERS, the IEEE ANTENNAS AND WIRELESS PROPAGATION LETTERS, IEEE ACCESS, the *IET Microwaves*, *Antennas and Propagation*, *Electronics Letters*, *Radioengineering*, *Microwave and Optical Technology Letters*, *International Journal of RF and Microwave Computer-Aided Engineering*, and *AEU-International Journal of Electronics and Communications*. He was a recipient of the Best Doctor's Dissertation Award of Liaoning Province, in 2013.

JIAN MA received the B.Eng. degree in electronic information engineering from Dalian Maritime University (DMU), Liaoning, China, in 2019, where he is currently pursuing the M.Eng. degree in information and communication engineering. His current research interests include balanced filters and power dividers.

HONGMEI LIU (Member, IEEE) received the Ph.D. degree in communication and information systems from Dalian Maritime University (DMU), China, in 2016. She is currently an Associate Professor with the School of Information Science and Technology, DMU. Her current research interests include passive microwave circuits, reconfigurable RF components, and CP microwave antennas. She is currently serving as a Technical Reviewer for the IEEE TRANSACTIONS ON INDUSTRIAL ELECTRONICS, the *Electronics Letters*, and *International Journal of RF and Microwave Computer-Aided Engineering*. She was a recipient of the Best Doctor's Dissertation Award of Liaoning Province, in 2017.

SHAOJUN FANG (Member, IEEE) received the Ph.D. degree in communication and information systems from Dalian Maritime University (DMU), China, in 2001. Since 1982, he has been at DMU, where he is currently the Head Professor with the School of Information Science and Technology. His recent research interests include passive RF components and antennas. He has authored or coauthored four books and over 100 journal articles and conference papers. He was a recipient of the Best Doctor's Dissertation Award of Liaoning Province, in 2002 and the Outstanding Teacher Award of the Ministry of Transport of China.